Surface defect engineered-Mg-based implants enable the dual functions of superhydrophobic and synergetic photothermal/chemodynamic therapy

Dongdong Zhang [a,b,c,d], Ru Xu [a], Shuhan Chen [a,b], Huihui Du [a,b], Shi Qian [a,b], Feng Peng [e,f,**], Xuanyong Liu [a,b,g,*]

a State Key Laboratory of High Performance Ceramics and Superfine Microstructure, Shanghai Institute of Ceramics, Chinese Academy of Sciences, Shanghai, 200050, China
b Center of Materials Science and Optoelectronics Engineering, University of Chinese Academy of Sciences, Beijing, 100049, China
c Shenzhen Key Laboratory for Innovative Technology in Orthopaedic Trauma, The University of Hong Kong Shenzhen Hospital, Shenzhen, China
d Center for Human Tissues and Organs Degeneration, Shenzhen Institutes of Advanced Technology, Chinese Academy of Science, Shenzhen, 518055, PR China
e Medical Research Institute, Department of Orthopedics, Guangdong Provincial People's Hospital (Guangdong Academy of Medical Sciences), Southern Medical University, Guangzhou, 510080, China
f GuangDong Engineering Technology Research Center of Functional Repair of Bone Defects and Biomaterials, Guangzhou, 510080, China
g School of Chemistry and Materials Science, Hangzhou Institute for Advanced Study, University of Chinese Academy of Sciences, 1 Sub-lane Xiangshan, Hangzhou, 310024, China

ARTICLE INFO

ABSTRACT

Promoting metallic magnesium (Mg)-based implants to treat bone diseases in clinics, such as osteosarcoma and bacterial infection, remains a challenging topic. Herein, an iron hydroxide-based composite coating with a two-stage nanosheet-like structure was fabricated on Mg alloy, and this was followed by a thermal reduction treatment to break some of the surface Fe–OH bonds. The coating demonstrated three positive changes in properties due to the defects. First, the removal of –OH made the coating superhydrophobic, and it had self-cleaning and antifouling properties. This is beneficial for keeping the implants clean and for anti-corrosion before implantation into the human body. Furthermore, the superhydrophobicity could be removed by immersing the implant in a 75% ethanol solution, to further facilitate biological action during service. Second, the color of the coating changed from yellow to brown-black, leading to an increase in the light absorption, which resulted in an excellent photothermal effect. Third, the defects increased the Fe^{2+} content in the coating and highly improved peroxidase activity. Thus, the defect coating exhibited synergistic photothermal/chemodynamic therapeutic effects for bacteria and tumors. Moreover, the coating substantially enhanced the anti-corrosion and biocompatibility of the Mg alloys. Therefore, this study offers a novel multi-functional Mg-based implant for osteosarcoma therapy.

1. Introduction

Osteosarcoma (OS) is a primary malignant tumor in the bone, which is difficult to detect in the early stage and has the characteristics of invasion, rapid development, and easy metastasis [1–3]. Clinically, after the surgical resection of the bone tumor tissue, chemotherapy/radiotherapy is required to clear the residual tumor cells to decrease neoplasm recurrence, and the resulting bone defect needs to be filled and repaired.[4] The disadvantage of chemotherapy/radiotherapy is that it can easily develop tolerance and cause systemic toxicity [3]. In addition, in a clinical setting, it was found that patients with bone tumors were prone to bacterial infections in the wound after tumor tissue resection due to the patients' poor immune system or patients with hyperglycemia and diabetes [4,5,6]. Thus, the design and construction

of bone filling materials with anti-tumor/anti-bacterial functions is of great significance in the treatment of OS in a clinical setting. Magnesium (Mg)-based materials have excellent osteogenic induction and biodegradability and suitable biomechanical properties, and, thus, they are considered a potential filling material for bone tumor therapy and the repair of defects [7–9]. Nevertheless, the rapid corrosion of Mg can easily cause excessive alkalinity and hydrogen gas (H_2) near the embedded surroundings [9]. This results in poor biocompatibility and premature loss of the mechanical properties of the implanted Mg materials. Therefore, in terms of bone tumor therapy for OS and Mg-based implants, both the requirements of biodegradation control and further therapeutic biofunctions should be considered. However, at present, the research and design of such Mg-based implants remain challenging.

A superhydrophobic surface has the properties of anti-corrosion, self-cleaning, and antifouling, which are beneficial for keeping medical implants clean and maintaining their anti-corrosion state before human use, such as during the transportation and storage stages [10–12]. However, superhydrophobic surfaces are not conducive to cell adhesion and the transfer of biochemical reactions [13]. To address this issue, Mg-based implants need a switchable superhydrophobic/hydrophilic property. This would allow for the functional Mg-based implants to maintain their superhydrophobic state before implantation into the human body but then the superhydrophobic property could be turned into a hydrophilic state by a certain method during operation. This would have significant clinical value but there are currently few reports on this aspect.

For antibacterial/anti-tumor purposes, current research mainly involves researchers loading functional reagents (such as ions, drugs, or biological reagents) onto the surface of materials [14–16]. However, the preparation process of the loaded coating is generally complex, and the loaded reagents are difficult to controllably release and, thus, may cause toxic side effects. Therefore, it is necessary to develop new modification strategies. The abnormal metabolism of tumor cells results in high hydrogen peroxide (H_2O_2) levels in the tumor tissue microenvironment (TME) [17]. Based on this, a variety of antitumor biomaterials with good peroxidase activity have been designed to catalyze H_2O_2 in the TME to produce reactive oxygen species for tumor chemodynamic therapy (CDT) [18]. Another strategy, photothermal therapy (PTT), has also been rapidly developed in recent years [19]. This refers to the method of killing tumors using local heating under light excitation. Both PTT and CDT have the advantages of accurate controllability and locally selective treatment. Thus, it may be promising to combine the functions of CDT and PTT on Mg-based implants for OS treatment.

In current researches, the modification of Mg-based implants mainly includes three aspects: alloying, amorphization, and surface modification. Alloying and amorphization treatment are beneficial for significantly improving the long-term corrosion resistance of magnesium implants [8]. In terms of the surface modification strategy for Mg-based materials, it is more favorable to integrate multi-functions as it has a lower cost [8]. Iron (Fe)-based materials appear more suitable as surface coatings for the fictionalization of Mg-based implants because they simultaneously possess the functions of biological safety and bone repair (osteogenesis and angiogenesis) and characteristics (photothermal and Fenton effects) related to tumor therapy [20–22]. Ferric oxyhydroxide (FeOOH) is a semiconductor material with a band gap of 2.1–2.6 eV, and it is composed of iron oxide (Fe–O) bonds and iron hydroxide (Fe–OH) bonds [23]. When compared to oxygen vacancy-mediated defects, limited research has been conducted on hydroxyl-mediated defects. Partial Fe–OH bond breaking will predictably cause three changes in performance: 1) the removal of the hydrophilic group –OH will result in a material change from hydrophilic to hydrophobic; 2) the generation of defects will reduce the band gap and increase light absorbance, which will further improve the PTT performance; and 3) the defects also cause divalent Fe and, thus, improve peroxidase-like activity, which in turn improves the performance of CDT.

Based on the above background and analysis, in this work, FeOOH nanosheets were prepared *in-situ* on a plasma electrolytic oxidation (PEO)/Mg–Fe layered double hydroxide (LDH) duplex coating modified-Mg alloy using an immersion process in Fe^{2+} solution. The composite coating exhibited a micro-nano sheet-like structure. Additionally, some of the Fe–OH bonds were broken by thermal treatment under a reducing atmosphere to cause surface defects. The defects enabled the Mg-based implants with "switchable" hydrophobicity and PTT/CDT response functions (Fig. 1). The effects of the surface defects on the properties of hydrophilicity, hydrophobicity, corrosion resistance, and biocompatibility were evaluated. Also, density functional theory (DFT) was applied to investigate the evolution of the band gap and Fenton reaction activity of FeOOH when some of the Fe–OH bonds were broken. In addition, the photothermal effect and peroxidase activity and their mediated PTT/CDT synergistic therapy were systematically studied.

2. Materials and methods

Materials. Commercial AZ31 rods were cut into the sheets with a diameter of 10 mm and a thickness of 2 mm as the raw substrates. The specimens were ground with 600 grit SiC paper and ultrasonically cleaned in absolute ethyl alcohol before use. Sodium glycerophosphate ($C_3H_7Na_2O_6P$, Sinopharm Chemical Reagent, China), Potassium hydroxide (KOH, Sinopharm Chemical Reagent, China), and Ferrous chloride ($FeCl_2 \cdot 4H_2O$, Sinopharm Chemical Reagent, China) were used to surface modify the AZ31 substrates.

Sample preparation. The synthesis processes for the various samples are shown in Fig. 2. The PEO process was carried out under a constant current mode at a current density of 0.4 A/cm², frequency of 1000 Hz, and duty cycle of 10%. The reaction lasted about 30 s at room temperature and was stopped at a voltage of 340 V. 4 L deionized water, which contained 40 g $C_3H_7Na_2O_6P$, 50 g KOH, and 35 g $KF \cdot 2H_2O$ as electrolytes. The AZ31 sheets and stainless steel were used as an anode and cathode, respectively. The as-prepared sample was defined as the PEO sample.

An Mg–Fe LDH film was fabricated onto the PEO coating through a two-step method of combining immersion and hydrothermal treatment. First, the PEO sample was immersed in 4 g/L of $FeCl_2 \cdot 4H_2O$ solution for 1.5 h. Second, the treated sample was placed in a Teflon-lined stainless vessel with water for 8 h at 120 °C. The as-prepared sample was defined as the LDH sample. The FeOOH samples were prepared by immersing the LDH sample in 2 g/L $FeCl_2$ $4H_2O$ solution for 4 h. Next, TR1-FeOOH and TR2-FeOOH were prepared by the thermal treatment of the FeOOH samples in an H_2/Ar (1/9) mixed reduced atmosphere at 150 °C for 90 and 180 min, respectively.

Surface characterization. The surface and cross-sectional topographies of samples were characterized by the scanning electron microscopy (SEM; S–3400 N, HITACHI, Japan). The chemical compositions of samples were investigated by energy dispersive spectrometry (EDS; IXRF-550i, IXRF SYSTEMS, USA). The crystal phase was measured by X-ray diffraction (XRD; D2PHASE, BRUKER, USA). The surface chemical state was investigated by X-ray photoelectron spectroscopy (XPS; RBD upgraded PHI–5000C ESCA system, USA). The Raman spectra were recorded via a confocal Raman microspectroscope (LabRAM, Horiba Jobin Yvon, France).

Water contact angle. The water contact angles of the samples were detected by a contact angle measurement (SL200B, Solon, china) by dropping a water droplet with a volume of 2 μL.

Self-cleaning and antifouling properties. The MgO nanopowder was used to cover the sample surface, and then the sample surface was washed with water to test the self-cleaning performance. Then, after immersing the sample in methylene blue solution, it was taken out to observe the stain of the sample to test its antifouling performance.

Superhydrophobic removal method. TR1-FeOOH and TR2-FeOOH samples immersed in 75% ethanol solution for 20 min to remove their surface superhydrophobicity. And, in the following tests, the superhydrophobicity of the TR1-FeOOH and TR2-FeOOH samples
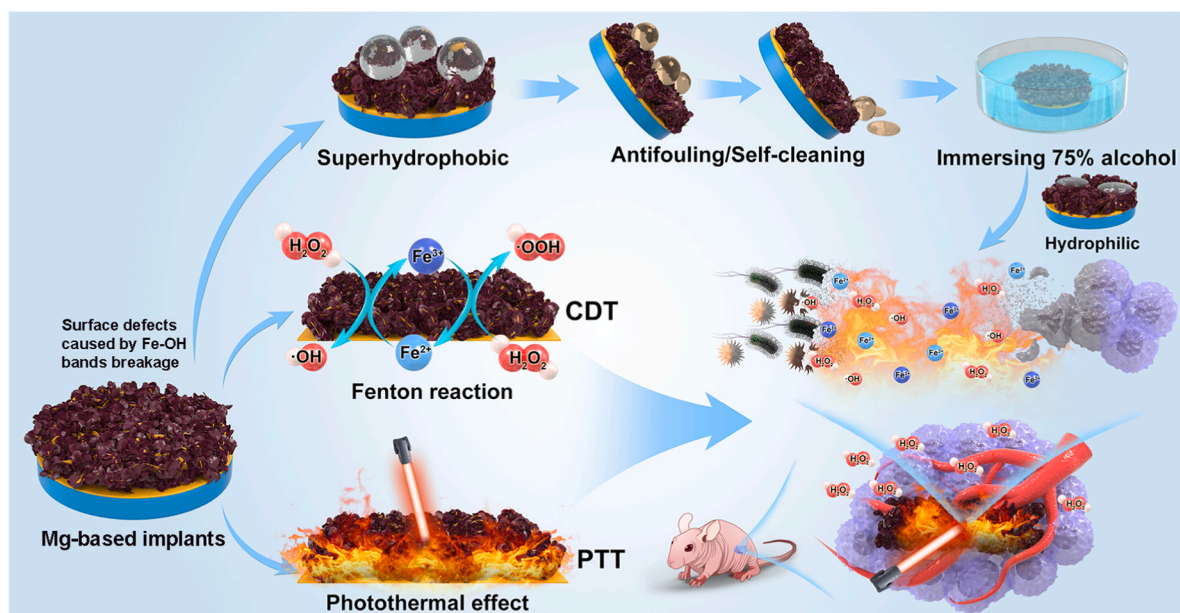
Fig. 1. A schematic diagram of the surface defects-engineered magnesium (Mg) alloy with the multi-functions of superhydrophobic and photothermal therapy (PTT)/chemodynamic therapy (CDT) effects and their mediated antifouling/self-healing abilities and anti-bacterial/tumor therapy, respectively.
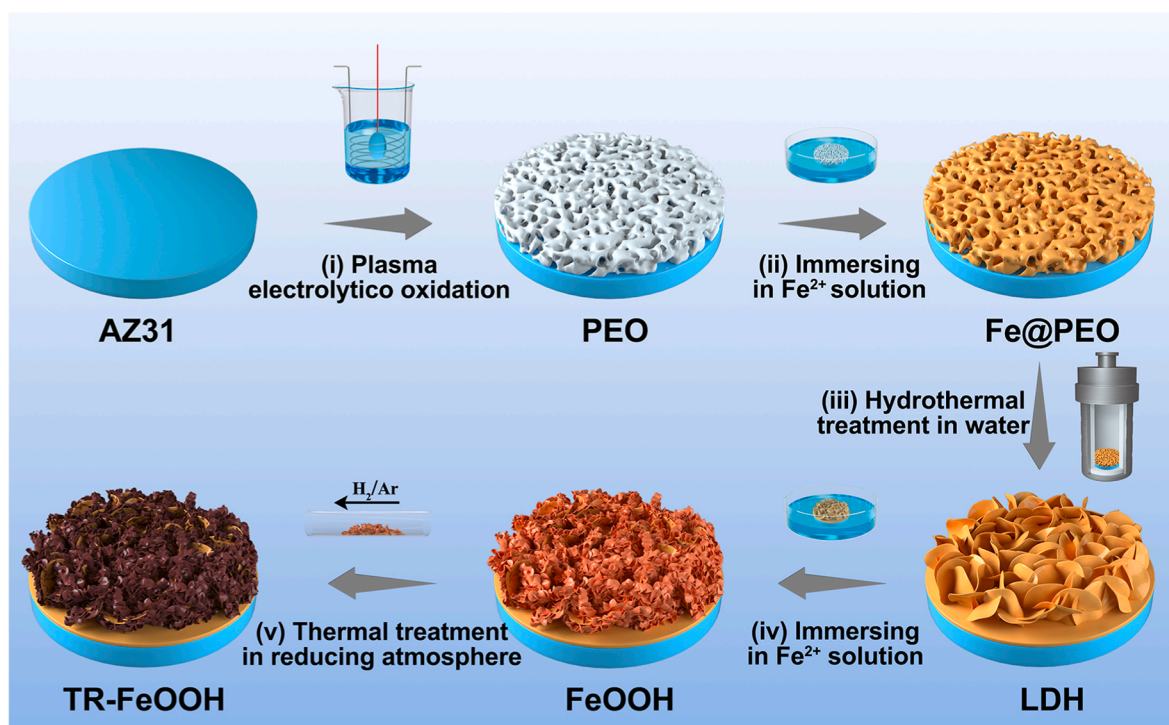
Fig. 2. A schematic illustration of the synthesis process for the various samples. Abbreviations: FeOOH, ferric oxyhydroxide; PEO, plasma electrolytic oxidation; LDH, layered double hydroxide.

was removed.

Corrosion tests. The samples were immersed in 4 mL of PBS solution at 37 °C, and the extracts were collected and fresh PBS solution was added each day. The pH values of all the extracts were measured using a pH meter. A hydrogen evolution test was carried out by placing the samples (four parallel specimens) in 300 mL of 0.9 wt% NaCl solution at 37 °C. Then, the released H was recorded. In addition, the samples were immersed in 2 mL of 0.9 wt% NaCl solution at 37 °C for 28 d, and then they were cleaned three times with ethanol. Afterward, the corrosion

morphology was observed by SEM.

Photothermal effect. The various samples were placed in a 24-well plate with 500 μL of phosphate-buffered saline (PBS) solution, and each well was irradiated using 808 nm NIR light ($1.0 \, W/cm^2$). Meanwhile, the corresponding temperature variation was record by a FLIR ONE infrared thermal instrument.

Oxidase-Like Activity Assessment. Oxidase-like activity of the samples were studied by evaluating the catalytic performance of 3,3′,5,5′-Tetramethylbenzidine (TMB) in 0.9 wt % NaCl solution. In

brief, saline solution with 4 mM TMB and 100 μM H_2O_2 (with or without) was added to the samples in a 24-well plate and co-incubated at room temperature for 10 min. Then, 100 μL of the mixture was transformed to a 96-well black plate and the absorbance from 500 nm to 800 nm was measured by Cytation 5 Multi-Mode Reader (BioTek, USA).

Density functional theory calculations. We have employed the Vienna Ab initio Simulation Package (VASP) to perform all density functional theory (DFT) calculations within spin-polarized frame. The elemental core and valence electrons were represented by the projector augmented wave (PAW) method and plane-wave basis functions with a cutoff energy of 400 eV. Generalized gradient approximation with the Perdew-Burke-Ernzerhof (GGA-PBE) exchange-correlation functional was employed in all the calculations. Geometry optimizations were performed with the force convergency smaller than 0.05 eV/Å. The DFT-D3 empirical correction method was employed to describe van der Waals interactions. For AFM of FeOOH, three cases are considered with the initial magnetic moments of Fe were set to be −5 or +5 μB (Fig. S1), which are parallel. And case 1 is most stable due to the lowest energy. Monkhorst-Pack k-points of $8 \times 8 \times 1$ were applied for the calculations. U-values, which are applied to d-orbitals of Fe is taken as 3.0 eV. All the atoms are relaxed in all the calculations.

3×3 supercell were applied to get the adsorption energy. Monkhorst-Pack k-points of $2 \times 3 \times 1$ was applied for the calculations. The Gibbs free energy (ΔG) for each electrochemical process is calculated as:

$$\Delta G = \Delta E + \Delta E_{ZPE} - T\Delta S$$

Where the value of ΔE, ΔE_{ZPE} and ΔS denotes the changes of DFT energy, the zero-point energy and the entropy at 300K, respective.

Hemolysis assay. All of the samples were immersed in saline solution for 30 min, then 30 μL of diluted blood (0.8 mL of whole blood was diluted with 1 mL of 0.9 wt % NaCl solution) was added into each sample and the co-incubated for 60 min at 37 °C. Meanwhile, 30 μL of diluted blood was added into saline solution and distilled water and incubated for 60 min as negative control and positive control, respectively. Subsequently, the solutions were centrifuged at 3000 rpm for 5 min. The absorbance of supernatants was detected by an enzyme-labeling (BioTek Cytation 5, USA) at 545 nm. The hemolysis rate (HR) was calculated as the following equation: Hemolysis = $(A_{sample}-A_{negative})/(A_{positive}-A_{negative})$.

Cytocompatibility. The osteoblast-like MC3T3-E1 cells were cultured in α-MEM at 37 °C with 5% CO_2. The proliferation rates of the cells (5.0×10^4 cells/mL) that were cultured in the various samples for 1, 4, and 7 d were measured using an AlamarBlue assay. The cells were seeded onto the various samples. After 4 d of culturing, the cells that adhered to the samples were fixed in 2.5 v% glutaraldehyde and dehydrated in ethanol. Afterward, their SEM morphologies were observed. Similarly, live/dead staining was studied by culturing cells on the samples for 4 d. Then, 100 μL of PBS solution mixed with live/dead staining kit containing calcein-AM and propidium iodide was added to each sample surface. Finally, the stained cells were observed by a fluorescence microscope using dark field mode (GX71, OLYMPUS, Japan).

Antibacterial properties. Each sample was incubated with 500 μL of bacterial (*E. coli* and *S. aureus*) suspension (10^7 CFU/mL, in saline) in a 24-well plate for 12 h. Then, the wells were exposed to 808 NIR (1.0 W/cm²) irradiation for 6 min, in NIR (+) groups. Afterward, all of the samples were transferred to tubes with 4 mL of 0.9 wt % NaCl solution and dissociated adhered bacteria. Then, the solutions were diluted 10 and 100 times for *E. coli* and *S. aureus*, respectively. Subsequently, the solution was spread onto standard agar culture plate and incubated for 18 h. Finally, the bacterial colonies were counted. In addition, bacteria on the samples were fixed by 2.5 v% glutaraldehyde and dehydrated in ethanol, and their bacterial morphology was observed by SEM. Furthermore, the bacterial were stained with LIVE/DEAD BacLight kit (L13152) and observed with a fluorescence microscope.

In vitro tumor therapy. The Sao-2 tumor cells (5.0×10^4 cells/mL) were seeded onto the surface of the samples in a 24-well plate for 4 d. Then, the wells were exposed to 808 NIR (1.0 W/cm²) irradiation for 10 min in NIR (+) groups. Afterward, the cell activity was measured using an AlamarBlue assay and live/dead staining.

In vivo tumor therapy. All manipulations conducted on animals herein adhered to the ARRIVE guidelines for animal experiments and were approved by the Guangdong Provincial People's Hospital (KY–N-2022-074-01). Fifteen Balb/c nude male mice (4–6 weeks) were used for the *in vivo* therapy. The 2×10^6 UMR106 tumor cells were subcutaneously injected into the right subaxillary of the mice, and then the mice were raised for 2–4 d to make sure that the tumor volume reached about 250 mm³. Before implantation, the mice were randomly assigned to five sample groups: AZ31, FeOOH, FeOOH-NIR(+), TR2-FeOOH, and TR2-FeOOH-NIR(+). The samples were implanted at the edge of the tumors near the skin incision. The NIR groups were irradiated with NIR and the temperature changes were monitored using an infrared imaging thermometer. The tumor volume and weight were recorded every day using the following formulae:

$$\text{tumor volume (V)} = (\text{length} \times \text{width}^2)/2$$

$$\text{relative tumor volume (Vr)} = V/V_0$$

where V_0 is the value of the tumor volume before implantation. The tumors were collected and photographed on day 7 after surgery. The tumors were then fixed in 4% formalin. After being embedded in paraffin, the tumors were sliced and stained with H&E, TUNEL, and Ki67. Moreover, for each group, the major organs of the mice were stained with H&E. For TUNEL staining, TdT, dUTP, and buffer (Servicebio) were mixed in a volume ratio of 1:5:50. Then the tissues were immersed in the mixed solution for 2 h at 37 °C. For Ki67 staining, the tissues were immersed in 3% H_2O_2 for 25 min, and then blocked by BSA for 30 min. After that, the tissues were sequentially stained by Ki67 (Servicebio) for 12 h and HRP- Goat anti-rabbit for 50 min, and finally immersed in DAB color development solution until the positive stained color appeared.

3. Results and discussion

3.1. Synthesis and characterization

Due to their low standard potential (−2.37 VS. SCE), Mg-based implants exhibit high surface chemical activity [24,25]. Therefore, first, minimizing the negative impact of rapid corrosion should be considered. Moreover, for the superhydrophobic coating, a rough structure is generally needed, especially a micro/nanostructure [26]. Based on these two considerations, the functional coating was designed with two layers as a pretreatment coating: 1) the PEO coating (denoted as PEO) was prepared as the underlayer due to its advantages of high bonding strength, wear resistance, and corrosion resistance; and 2) the Mg–Fe LDH nanosheets were grown *in-situ* on the PEO coating as a middle layer to construct the first-order rough sheet-like structure. The PEO/Mg–Fe LDH composite coating (denoted as LDH) was studied in a previous study [25]. Then, the FeOOH nanosheets were prepared on the Mg–Fe LDH nanosheets using the immersion method, and the surface defects were caused by thermal treatment in a reduced atmosphere.

The formation process of the FeOOH nanosheets can be described as an alkaline-induced self-assembly process. The Mg–Fe LDH belongs to an alkaline hydroxide that precipitates Fe^{2+} close to the surface to form $Fe(OH)_2$ during the immersion process (Eq. (1)). Then, $Fe(OH)_2$ transforms to FeOOH through a natural oxidation process with oxygen (Eq. (2)).

$$Fe^{2+} + 2OH^- \rightarrow Fe(OH)_2 \tag{1}$$

$$4Fe(OH)_2 + O_2 \rightarrow 4FeOOH + 2H_2O \tag{2}$$

It should be noted that the comprehensive performance of PEO-treated AZ31 is significantly better than bare AZ31 [8,9]. Therefore, the PEO sample was selected as the control group. The surface and cross-sectional morphologies of the various samples were observed using scanning electron microscope (SEM), as shown in Fig. 3. The PEO sample presented with a typical porous structure, and the thickness of the coating was approximately 4.1 μm. Many nanosheets sealed the porous structure when the LDH film grew *in situ*, and the thickness increased to approximately 7.8 μm. For the FeOOH sample, interestingly, many of the small nanosheets grew on the larger LDH nanosheets that formed a two-stage surface micro/nanostructure. Additionally, the Fe content increased from approximately 8.2 ± 0.4 to 15.0 ± 0.6 at.%. After the thermal reduction treatment, the structure, thickness, and Fe content of the composite coating did not change significantly. However, the color of the specimens changed from reddish-brown to brownish-black. This may have been caused by lattice defects in the coating, resulting in increased light absorption capacity.

The X-ray diffraction (XRD) patterns were tested to survey the evolution of the surface crystalline phase after each treatment, as displayed in Fig. 4a. Due to the PEO/Mg–Fe LDH composite coating as the pretreatment coating, the magnesium oxide (MgO) and LDH phases were detected on each modified specimen. The small FeOOH nanosheets had decreased detection intensity for the LDH phase. Furthermore, the FeOOH phase was detected in the FeOOH and TR1-FeOOH samples but not in the TR2-FeOOH sample, suggesting that the excessive thermal reduction treatment highly affected its crystallinity and caused lattice defects in the FeOOH phase. Moreover, the Raman spectrum of the

FeOOH, TR1-FeOOH, and TR2-FeOOH samples was recorded (Fig. 4b). The peaks that were detected at 213.8, 279.4, and 371.6 cm^{-1} were attributed to the FeOOH phase [23]. These peaks did not obviously change after the thermal reduction treatment.

Then, X-ray photoelectron spectroscopy (XPS) was used to investigate the surface chemical states of the samples, and the results are displayed in Fig. 4c–i. Only Mg, Fe, and oxygen (O) were detected in the survey spectra of the modified groups. The O 1s spectra of the FeOOH, TR1-FeOOH, and TR2-FeOOH samples were divided into peaks that were centered at approximately 529.9 and 531.2 eV, belonging to the Fe–O and Fe–OH bands, respectively [27,28]. The intensity of the Fe–OH band of the samples was in the order of FeOOH > TR1-FeOOH > TR2-FeOOH, reflecting that part of the surface Fe–OH band was breaking after the thermal reduction treatment. The Fe 2p spectra of these samples had two main peaks. Each peak could be divided into two peaks belonging to Fe^{3+} and Fe^{2+}, respectively. From these results, it can be seen that the content of Fe^{2+} on the surface of TR1-FeOOH and TR2-FeOOH was higher than that on the FeOOH sample. According to the fitting results, the Fe^{2+}/Fe^{3+} ratio of FeOOH, TR1-FeOOH, and TR2-FeOOH samples is 1.87, 2.23, and 2.28, respectively. After the thermal reduction treatment, the partial fracture of the Fe–OH bond on the surface of the TR1-FeOOH and TR2-FeOOH samples led to an increase in the Fe^{2+} content. Collectively, these results confirm that the FeOOH nanosheets were grown *in situ* on the PEO/Mg–Fe LDH coated Mg alloys and the surface presents with a micro/nanostructure. Moreover, the surface defects can be easily controlled by the thermal reduction treatment.
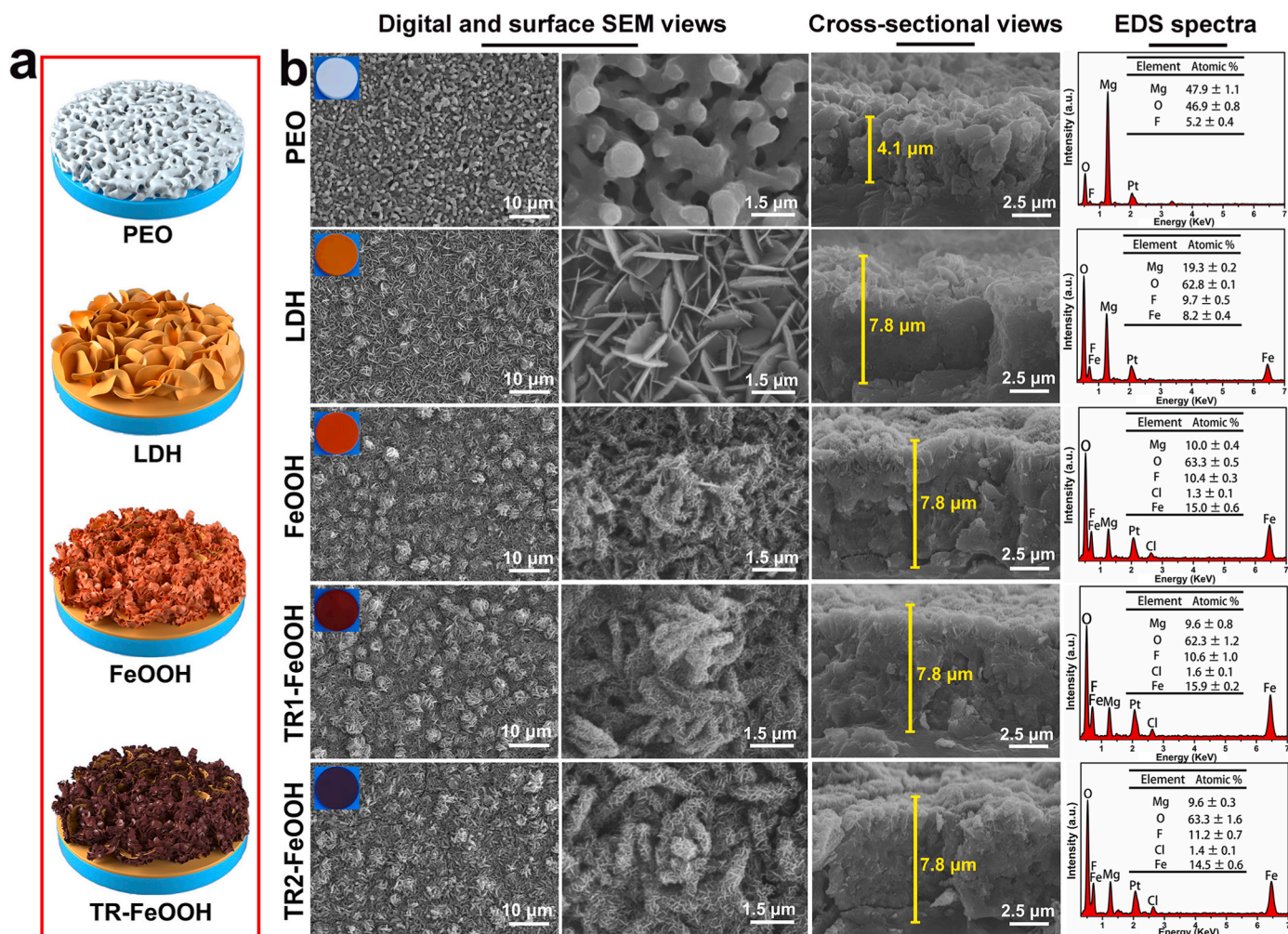
Fig. 3. Schematic diagram of coating structure (a); Digital photographs, surface morphologies, cross-sectional views and EDS spectra of the various samples (b).
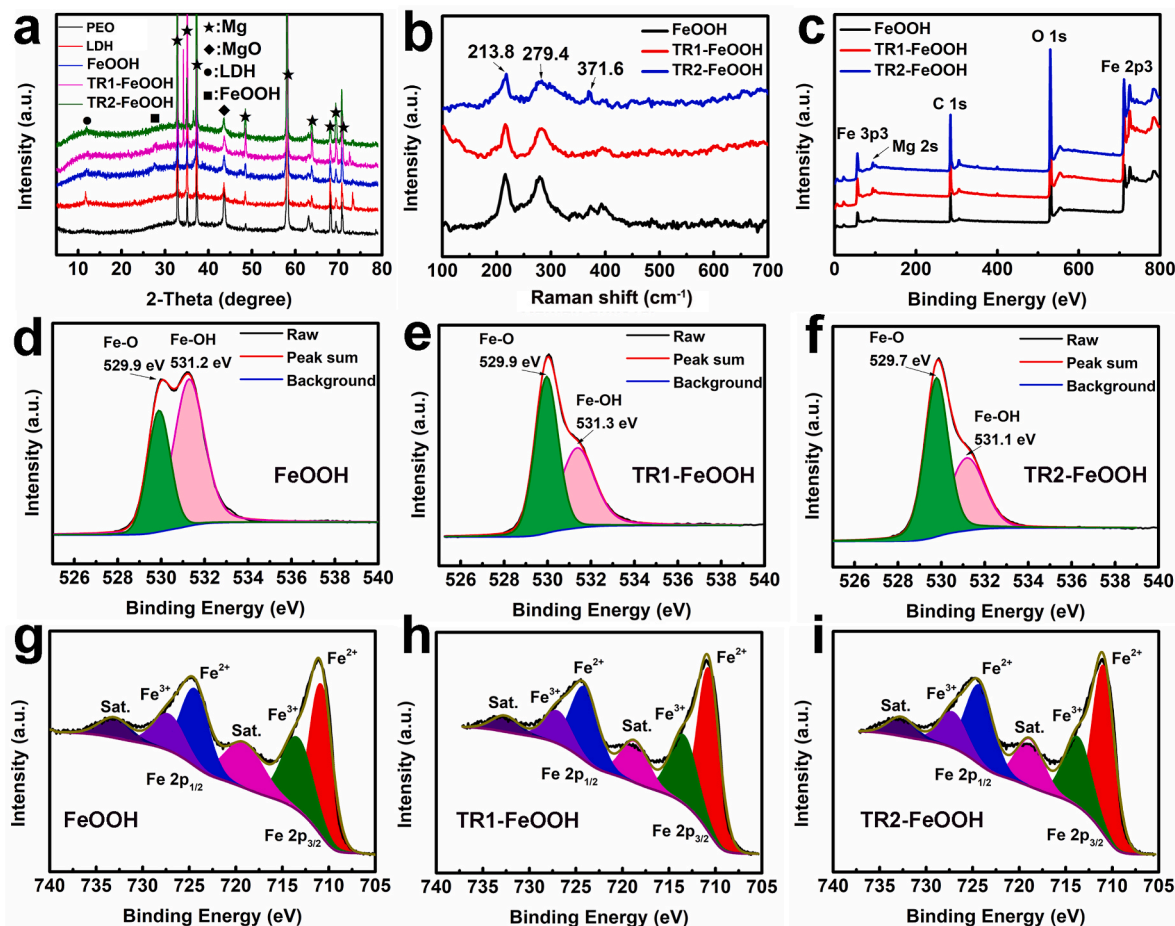
Fig. 4. The XRD patterns (a), Raman spectra (b), survey XPS spectra (c), and high-resolution XPS spectra for the oxygen (O) 1s (d–f) and iron (Fe) 2p (g–i) of the different samples.

3.2. Superhydrophobic functions and the removal method

Fig. 5a shows the initial contact angles of the various samples. The water contact angle of the PEO, LDH, and FeOOH samples was approximately 10°, which is hydrophilic. The water contact angle of the TR1-FeOOH and TR2-FeOOH surfaces was approximately 142° and 151°, respectively. The TR2-FeOOH surface exhibited a super-hydrophobic state (contact angle greater than 150°). In addition, the time-varying contact angles on the surface of the TR1-FeOOH and TR2-FeOOH samples in the air were tested to evaluate superhydrophobic stability. The contact angle did not obviously change after 7 days of being placed in an air environment (Fig. 5b), indicating good stability.

The obvious increase in the contact angle of the TR1-FeOOH and TR2-FeOOH samples was related to the reduction in Fe–OH bind on their surface after the heat treatment. The hydroxyl groups are hydrophilic, and FeOOH without the heat treatment contained abundant surface hydroxyl groups, which made it appear to have a hydrophilic surface. After the heat treatment in a reduced atmosphere, the hydroxyl groups on the surface decreased, resulting in the change from a hydrophilic state to a hydrophobic state. Additionally, the surface exhibited a rough micro/nano-sheet structure, which enhanced the hydrophobic effect and promoted the transition of the sample to a superhydrophobic state. Superhydrophobic surfaces can prevent water molecules from contacting the coating and improve its corrosion resistance.

Furthermore, the superhydrophobic surface also has the functions of self-cleaning and antifouling. Fig. 5c shows the self-cleaning performance test for the TR2-FeOOH sample. The sample surface was polluted with MgO nanopowder, and then water droplets were sprayed onto the sample surface with a syringe that was filled with ultrapure water. The water droplets did not wet the sample surface but were in a water column or water droplet state, which could quickly remove the surface MgO nanopowder and showed excellent self-cleaning performance. Fig. 5d displays the antifouling test for the TR2-FeOOH sample. The PEO, FeOOH, and TR2-FeOOH samples were immersed in methylene blue solution. However, unlike the PEO and FeOOH samples which were stained with blue stains, the TR2-FeOOH sample retained a clean surface. Overall, the superhydrophobicity of the TR2-FeOOH sample could prevent water molecule corrosion and dust pollution during storage, transportation, and other parts of the supply chain.

Nevertheless, the superhydrophobic surface of the materials is usually not conducive to the early adhesion of cells and the exchange of information between the coating of the cells and tissues [13]. Therefore, it is difficult for it to play a specific biological function. Thus, it is necessary to remove the superhydrophobic property of the material before it is implanted into the body. Fig. 5e shows the contact angle changes in the TR1-FeOOH and TR2-FeOOH samples which were immersed in 75% ethanol solution. Before biological experiments, the samples need to be sterilized. Immersion in 75% ethanol solution is one of the most used sterilization methods. When the samples were immersed in the 75% ethanol solution for 5 min, the two groups of samples lost their hydrophobic state. Then, when soaked for 20 min, the contact angle of both groups of the samples was lower than 50°. Generally, the hydrophobic material surface is lipophilic. Thus, immersing the TR1-FeOOH and TR2-FeOOH samples in the 75% ethanol solution containing the oil and water phases resulted in the water molecules rapidly wetting the surface of the samples and the loss of their
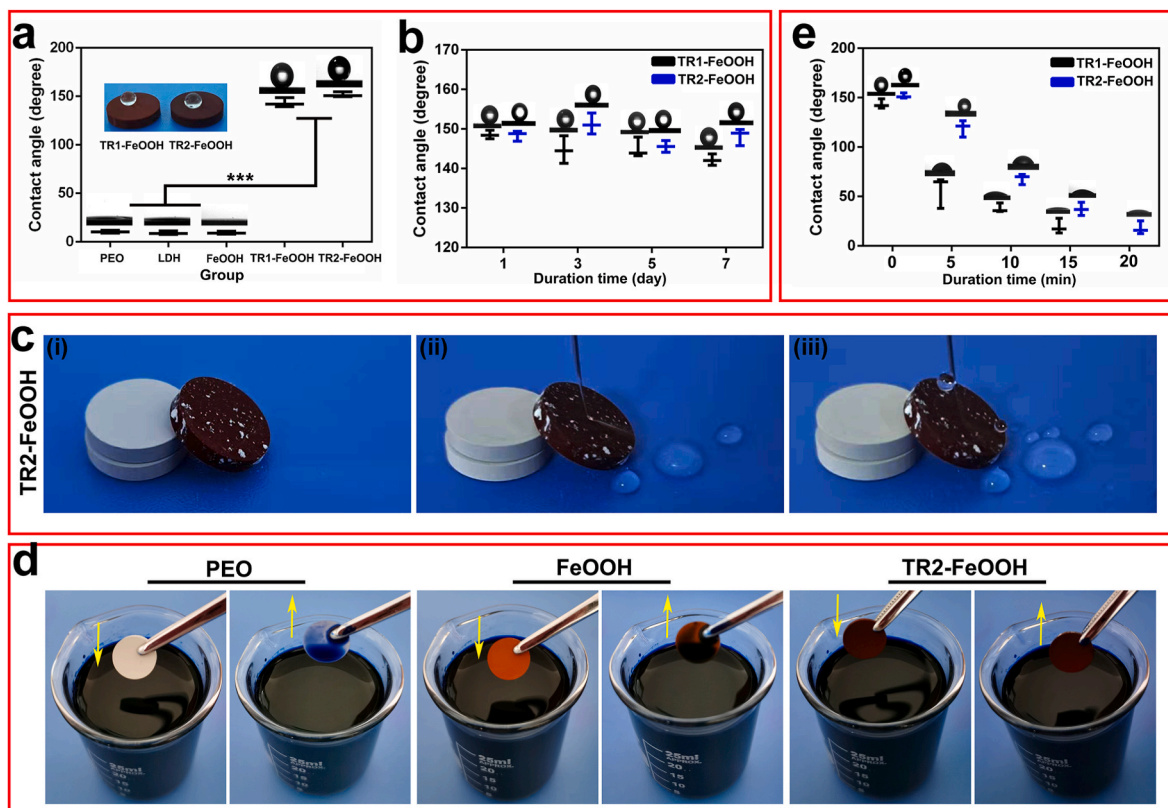
Fig. 5. The static contact angels of the various samples (a); contact angle evolution of the TR1-FeOOH and TR2-FeOOH samples in the air for various time periods (b); self-cleaning tests for the TR2-FeOOH sample (c); antifouling test for the PEO,FeOOH, and TR2-FeOOH samples (d); and contact angle evolution of the TR1-FeOOH and TR2-FeOOH samples in a 75% ethanol solution for various time periods (e).
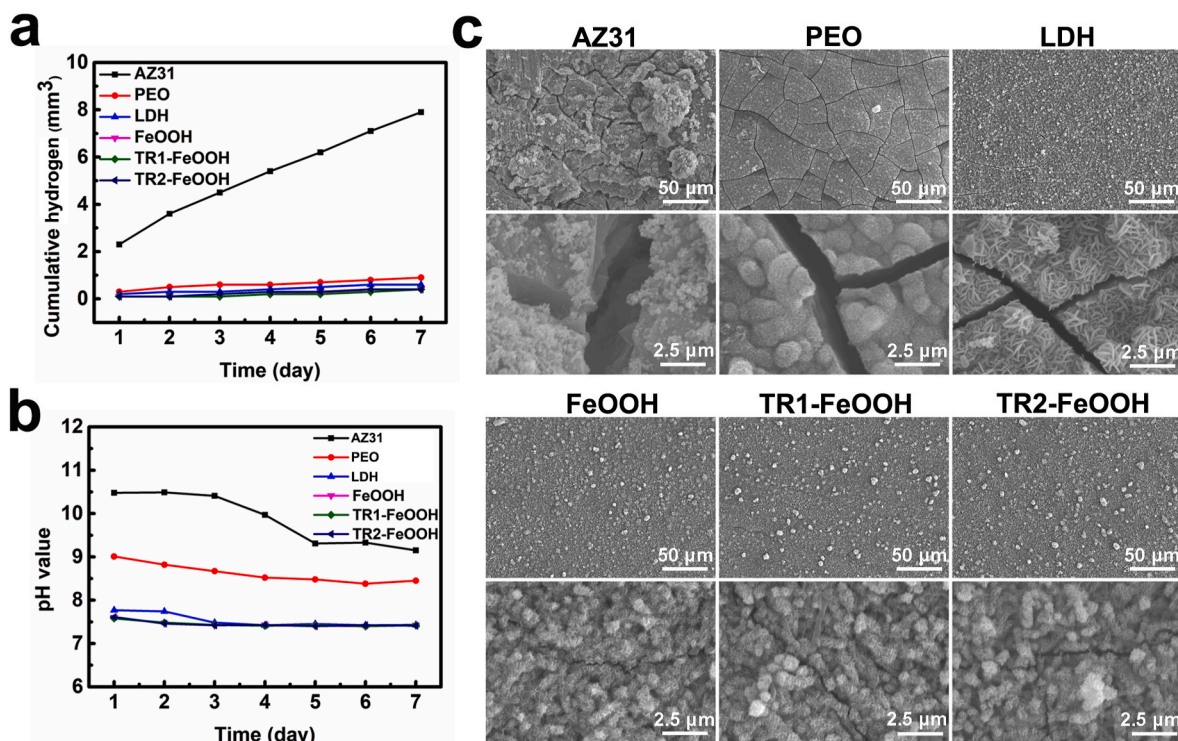
Fig. 6. The corrosion resistance evaluation: (a) the cumulative hydrogen that was released during sample corrosion, (b) pH value evolution, (c) and corrosion morphologies of the various samples that were immersed in saline for 28 d.

superhydrophobic properties. Therefore, the TR1-FeOOH and TR2-FeOOH samples can change from a hydrophobic state to a hydrophilic state when sterilized with a 75% ethanol solution. Consequently, in the following tests, the superhydrophobicity of the TR1-FeOOH and TR2-FeOOH samples was removed to better simulate its actual use.

3.3. Corrosion resistance

The corrosion resistance of the samples immersed in saline or PBS solution was evaluated to simulate their corrosion behavior of samples in human body after the superhydrophobic was removed. Fig. 6a displays the H_2 evolution behavior of each group. All the coatings significantly reduced the H_2 release of the Mg substrate but there was no obvious disparity between the coatings. Fig. 6b shows the pH value changes in the extracts of the various samples. The AZ31 and PEO groups exhibited a high pH value during the test period, indicating fast corrosion of the Mg substrate. In contrast, the other coatings had a slight influence on the change in the pH value, which is consistent with the results of H_2 evolution. Furthermore, the corrosion morphology of each sample when immersed in 0.9 wt% NaCl for 28 d was characterized using SEM (Fig. 6c). Many large cracks appeared in the AZ31 and PEO groups and some small cracks were observed in the LDH group. However, the surfaces of the FeOOH, TR1-FeOOH, and TR2-FeOOH groups better maintained their integrity, revealing their better corrosion resistance. The PEO coating is porous, therefore, once the corrosive fluid permeated through the pores and induced cracks, the cracks expanded quickly [29], resulting in large-scale widening of the cracks across the coating, and this is shown in the low magnification image of the PEO group in Fig. 6c. Thus, further deposition of a layer on the LDH structure

could significantly decrease the cracks. Nevertheless, because the sheets of the LDH structure were large, there were still gaps where the corrosive fluid could penetrate. Hence, a few cracks were also observed at high magnification. For the FeOOH, TR1-FeOOH, and TR2-FeOOH samples, the nanostructures were formed on the LDH sheets, which could sufficiently prevent the penetration of the fluid. Therefore, only a few small cracks were observed at high magnification, and only a few released H_2 and pH value changes were detected. In addition, all of coatings exhibit better adhesion stability than PEO coating (Fig. S2).

3.4. Photothermal and chemodynamic effect

The light adsorption ability of the samples is shown in Fig. 7a. In comparison with the other samples, the absorbance of the TR1-FeOOH and TR2-FeOOH samples presented with distinct enhancement from 450 to 850 nm due to their increased deficiency. According to the Kubelka–Munk function, the bandgap of FeOOH, TR1-FeOOH, and TR2-FeOOH was 1.98 eV, 1.74 eV, and 1.62 eV, respectively (Fig. S3). With better light adsorption ability, the TR1-FeOOH and TR2-FeOOH samples exhibited a higher increase in temperature under near infrared light irradiation (NIR) (Fig. 7b). Moreover, the cyclic photothermal curve of TR2-FeOOH revealed that it not only possessed excellent photothermal-conversion performance but also had good repeatability during recycling (Fig. 7c). A TMB chromogenic assay was carried out to investigate the oxidase-like and peroxidase-like activities of the various samples. Without H_2O_2, the TR1-FeOOH and TR2-FeOOH samples showed certain oxidase-like activity, as revealed by the increased absorption intensity of TMB at 652 nm (Fig. 7d). Therefore, the oxidative activity of the TR1-FeOOH and TR2-FeOOH samples might favor their ability against
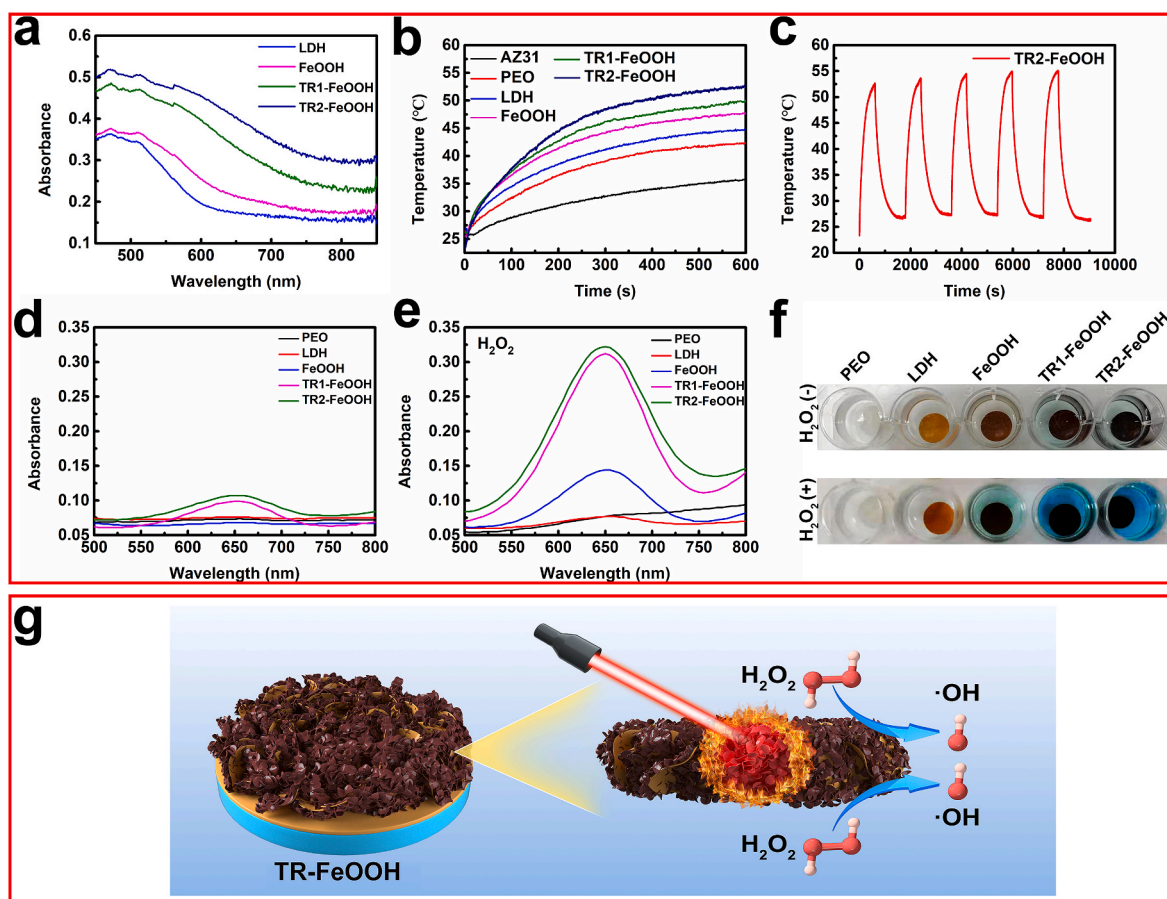
Fig. 7. The ultraviolet absorption spectra (a), temperature-elevation curves (b), and photothermal on-off effects (c) of the various samples. The catalytic oxidation performance of TMB for the various samples with (d) or without (e) 100 μM hydrogen peroxide (H_2O_2) and the corresponding digital photographs (f). A schematic illustration of TR2-FeOOH for the hyperthermia-enhanced Fenton reaction (g).

tumor cells and bacteria. In the presence of H_2O_2, enhanced catalytic activity was observed in the FeOOH, TR1-FeOOH, and TR2-FeOOH samples (Fig. 7e), especially in the TR2-FeOOH sample. This indicates the superior catalytic activity of TR2-FeOOH in generating highly oxidative ·OH *via* the Fenton reaction. The images of TMB, which was catalyzed by various samples with and without H_2O_2, are shown in Fig. 7f, and they were used to clarify the above conclusions. The ion, Fe^{2+}, is widely known as a Fenton reagent with the ability to catalyze H_2O_2 to oxidative ·OH [30,31]. In this study, the Fe in the FeOOH sample endows it with catalytic ability, especially in the presence of H_2O_2. After the thermal reduction treatment, many defects were introduced into FeOOH; therefore, the TR1-FeOOH and TR2-FeOOH samples exhibited much higher catalytic performance. Consequently, the above data suggest that the defect-rich TR2-FeOOH samples possess favorable photothermal and catalyze activities, as depicted in Fig. 7g.

To further understand the excellent photothermal performance and enzyme-like catalyze activity of the vacancy-rich TR-FeOOH samples, the DFT calculation was conducted. The slab model of FeOOH and FeO $(OH)_{1-x}$ was established (Fig. 8a). When compared to FeOOH, it is notable in Fig. 8b and c that several narrow bands of $FeO(OH)_{1-x}$ lie above the Fermi level, with a smaller bandwidth. These narrow bands could contribute to the better adsorption of $FeO(OH)_{1-x}$ than that of FeOOH in the range of near-infrared to visible light, corresponding to the results of Fig. 8a, which show the strong photothermal performance of $FeO(OH)_{1-x}$ [32]. Moreover, the narrow band gap would have enhanced the conductivity $FeO(OH)_{1-x}$ and accelerated the charge transportation of the enzyme-like catalytic process. In contrast, the adsorption of H_2O_2 on the surface of the catalyst was the first step of the peroxidase-like catalytic reaction, and then the transition state OH was obtained. As demonstrated in Fig. 8d, the transition state OH could combine with the H atom to generate water (H_2O), which indicated that

the transition state OH could not exist on the optimized surface of FeOOH. However, this phenomenon could not be observed on the surface of $FeO(OH)_{1-x}$, therefore, ·OH was obtained on the surface of FeO $(OH)_{1-x}$. Furthermore, the free energy diagrams for the peroxidase-like catalytic reaction on both sites were acquired by calculating the free energies of the adsorbed intermediates of these models. According to Fig. 8e, the adsorption of H_2O_2 on the surface of FeOOH or $FeO(OH)_{1-x}$ was considered as the rate-determine step where H_2O_2 dissociated into ·OH. The H_2O_2 adsorption energy of $FeO(OH)_{1-x}$ was lower than that of FeOOH, which means that the adsorption ability of H_2O_2 by $FeO(OH)_{1-x}$ was stronger than that of FeOOH. Thus, more ·OH would have been generated on the surface of $FeO(OH)_{1-x}$ than FeOOH, revealing the better peroxidase-like catalytic activity of $FeO(OH)_{1-x}$ [33,34].

3.5. Biocompatibility

The hemolysis rate is a key parameter that should be below 5% for clinical application. The AZ31 specimen possessed a high hemolysis rate which was >5% (Fig. 9a). Fortunately, after the coating protection, the hemolysis rate of the other groups was reduced to <5%. The proliferation rate of the MC3T3-E1 cells that were cultured on the various samples was measured using an AlamarBlue assay, as displayed in Fig. 9b. The cells that were cultured on the LDH, FeOOH, TR1-FeOOH, and TR2-FeOOH samples had a similar proliferation behavior and were all higher than that of the PEO group. This indicates that the prepared Fe-based coatings possess excellent biocompatibility. To verify this result, the SEM morphology and live/dead staining of the cultured cells on the various samples were observed after 4 d. As shown in Fig. 9c, only part of the PEO surface was covered by living cells, whereas almost the total surface of the LDH, FeOOH, TR1-FeOOH, and TR2-FeOOH samples was covered by living cells, suggesting their superior cytocompatibility, and
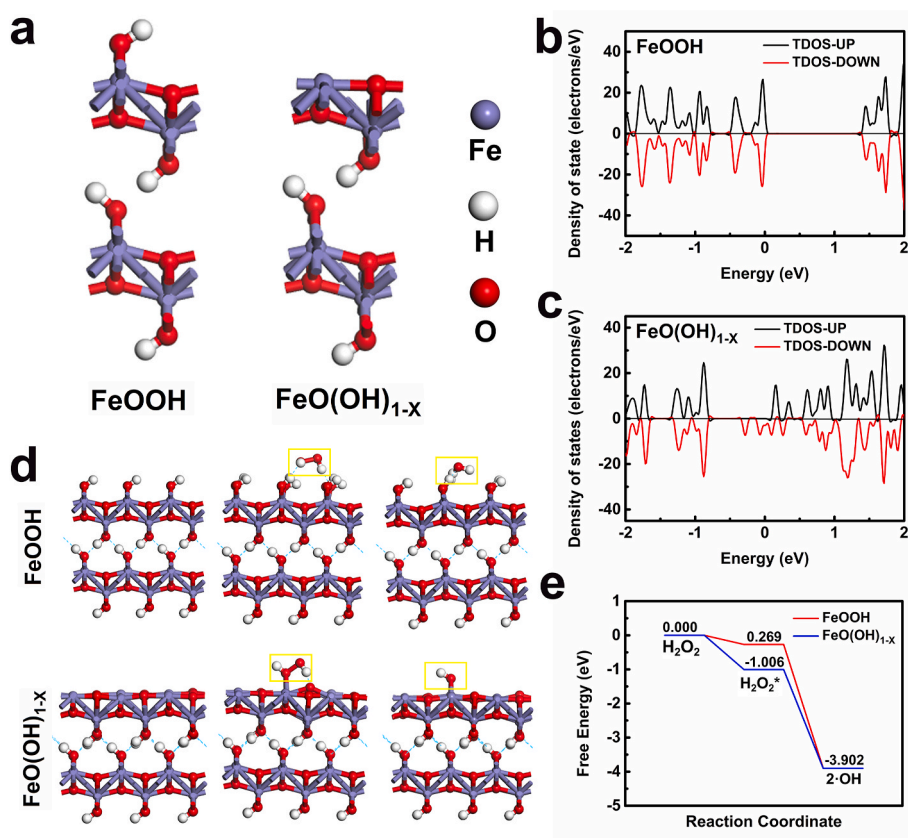
Fig. 8. The optimized model of ferric oxyhydroxide (FeOOH) and $FeO(OH)_{1-x}$ (a). The total density of state (DOS) analysis of FeOOH (b) and $FeO(OH)_{1-x}$ (c). The reaction pathways of the activation of hydrogen peroxide (H_2O_2) which generates ·OH on the surface of FeOOH and $FeO(OH)_{1-x}$ (d). The Gibbs free-energy diagram of the peroxidase-like catalytic reaction process of FeOOH and $FeO(OH)_{1-x}$ (e).
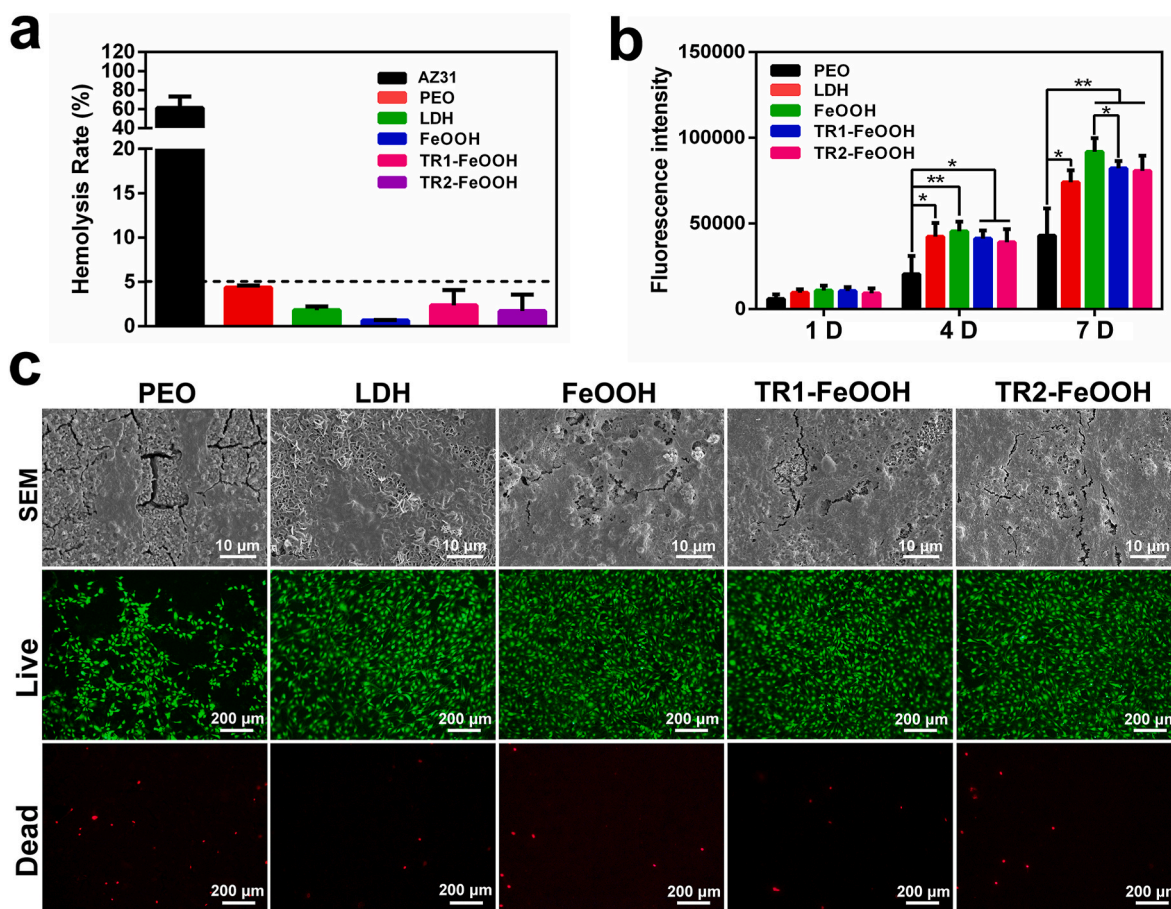
Fig. 9. The *in vitro* biocompatibility evaluations: (a) the hemolysis ratio; (b) fluorescent intensity of AlamarBlue which was reduced by the MC3T3-E1 cells that were cultured on the various samples for 1, 4, and 7 d; (c) the SEM images and fluoroscopy images of the live/dead (green/red) staining of the MC3T3-E1 cells that were cultured on the various samples for 4 days.

this is consistent with the results for cell proliferation. The biocompatibility of Mg-based implants is highly reliant on their corrosion resistance. With poor corrosion protection, excessive Mg ions and OH$^-$ are released along with the degradation of the Mg substrate, resulting in an extortionate osmotic pressure and pH value [23,35]. This causes irreversible damage to the erythrocytes and tissue cells. In this study, LDH and FeOOH coated PEO provided significant protection for the Mg substrate (Fig. 6), and a further thermal reduction process had little influence on its corrosion resistance. Hence, all the multi-layer coated Mg samples exhibited favorable hemocompatibility and cytocompatibility.

3.6. Antibacterial effect

The antibacterial effects of the reduced LDH/FeOOH coatings against both Gram-positive *Staphylococcus aureus* and gram-negative *Escherichia coli* were investigated using a bacterial plate method and the results are shown in Fig. 10a. Due to the poor corrosion resistance and biocompatibility of the PEO coating, few bacterial colonies grew in the PEO sample. In contrast, with highly improved biocompatibility, the LDH and FeOOH samples also had relatively weak antibacterial efficiency. Fortunately, benefiting from the chemodynamic effect, the bacterial colonies decreased in the TR1-FeOOH and TR2-FeOOH samples. Due to the presence of more Fe^{2+} in the TR1-FeOOH and TR2-FeOOH samples, more ROS can be generated to cause oxidative damage to bacteria. Furthermore, in the presence of NIR light, almost all the bacteria on the TR1-FeOOH and TR2-FeOOH samples were killed. The bacterial morphology and membrane integrity were observed using SEM to verify

the results (Fig. 10b). Without light irradiation, the *S. aureus* and *E. coli* attached to the surface of all the samples and presented with relatively integrated spherical and rod morphology, respectively. After irradiation, both the *S. aureus* and *E. coli* membranes experienced partial shrinking (yellow arrow) and were damaged. The damaged bacterial membranes result in the leakage of cytoplasm and interruption of ATP synthesis, thus, leading to bacterial death [36]. In addition, live/dead staining was used to further confirm the antibacterial effects of the various samples, and the fluorescent images of *S. aureus* are displayed in Fig. 10c. Without irradiation, the bacteria on the sample were dyed green (alive), and the fluorescence intensity in the TR1-FeOOH and TR2-FeOOH samples was much lower than that of LDH and FeOOH, indicating their better antibacterial efficiency. Moreover, upon NIR light irradiation, the green fluorescence changed to red fluorescence (dead), indicating that the bacteria were killed. The above results demonstrate that the reduced LDH/FeOOH coatings could inhibit bacteria proliferation through the chemodynamic effect alone, and with NIR irradiation, the bacteria were all killed under the synergistic actions of the chemodynamic and photothermal effects.

3.7. Osteosarcoma destruction

For *in vitro* therapeutic evaluation, osteosarcoma cells (Saos-2) were seeded on various samples for 4 days, and then treated the adhered cells with or without NIR light irradiation. Without irradiation, the number of cells on the LDH surface increased compared with that on PEO, because LDH nanosheets significantly improved the corrosion resistance and biocompatibility of the PEO sample (Fig. 11a). However, the cell
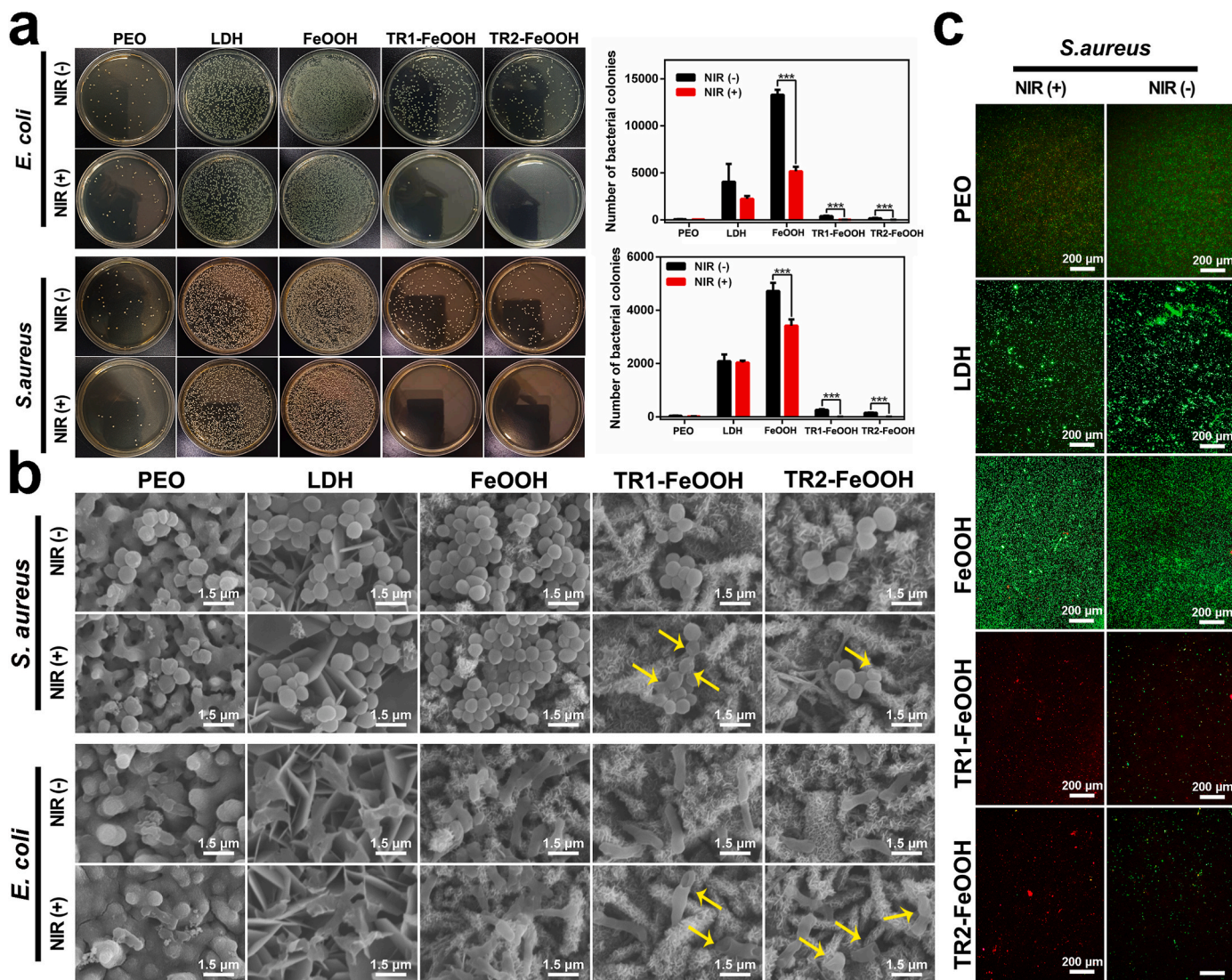
Fig. 10. The *in vitro* antibacterial investigation: (a) the representative culture images of the bacterial colonies and corresponding bacterial colony counts; (b) SEM morphologies of the bacteria in the various samples under different treatments, with the damaged membranes indicated with yellow arrows; (c) and live/dead staining of *Staphylococcus aureus* in the various samples.

number decreased after the LDH structure was modified with FeOOH nanosheets, and further decreased after it was thermal reduced. This is because FeOOH and TR-FeOOH showed peroxidase-like activity, which can catalyze the conversion of H_2O_2 to strong oxidizing ·OH radical and thus doing damage to the cells. The qualitative and quantitative results of ROS levels for tumor cell can prove this explanation (Fig. S4). Compared to samples FeOOH sample, there is more divalent iron on the surfaces of TR1-FeOOH and TR2-FeOOH samples, indicating a relatively strong killing effect on tumor cells. NIR irradiation had few influences on the cell proliferation of the osteosarcoma cells cultured on PEO, and FeOOH surfaces. However, under NIR irradiation, the cells cultured on TR-FeOOH surfaces were completely killed. To clearly visualize the Live/Dead cell distributions, the cells were further stained with calcein-AM and PI (Fig. 11b). It can be seen that almost no dead cells were observed for all the groups when no NIR irradiation. Under NIR irradiation, there a few dead cells were observed on LDH and FeOOH surfaces, whereas only dead cells and no living cells were found on TR1-FeOOH and TR2-FeOOH samples. This suggested that reduced FeOOH coatings exhibited excellent NIR-induced anti-tumor ability, which is consistent with the proliferation results.

The *in vivo* anti-tumor ability of TR2-FeOOH was evaluated using a

subcutaneously tumor model in mice. As shown Fig. 11c and d, higher temperature was detected surrounding TR2-FeOOH implant when irradiate with NIR than that of FeOOH implant, which indicated superior photothermal effect of TR2-FeOOH implant *in vivo*. The obtained tumor tissue and monitored tumor size during the experiment are displayed in Fig. 11e and f, respectively. For AZ31, FeOOH, and TR2-FeOOH groups, at day 7 after surgery, the tumor size was approximately 5 times larger than raw tumor size. However, tumor almost stopped grow up for FeOOH-NIR(+) group and was significantly smallest than that of AZ31, FeOOH, and TR2-FeOOH groups. Further, the tumor showed a slightly decrease in size for TR2-FeOOH-NIR(+) group. Nevertheless, the body weight record suggested that no significant difference was detected for all the groups, revealing photothermal therapy would not affect mice status. In addition, H&E, Ki67, and TUNEL staining was conducted to evaluate the anti-tumor ability of TR2-FeOOH implant at histological level and the results are shown in Fig. 11h. Few tumor-cell nuclei were observed for NIR irradiation groups, especially for TR2-FeOOH-NIR(+) group. Ki67 is a cell proliferation-associated antigen and TUNEL assay is always used to evaluate apoptosis of tumor cells. Smallest area of Ki67 positive stained (marked by brown) whereas largest area of TUNEL positively stained (marked by blue) were found for TR2-FeOOH-NIR(+)
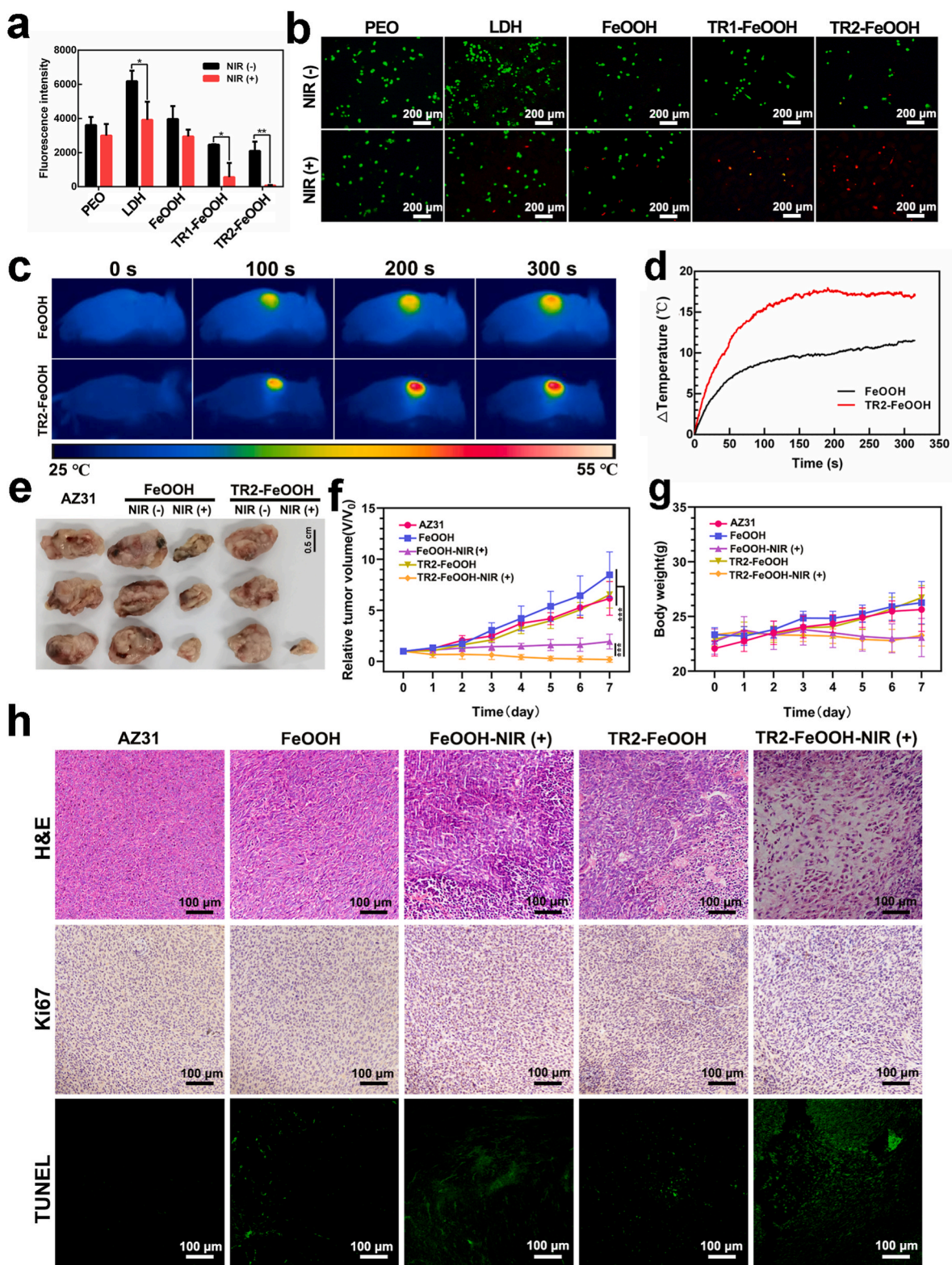
Fig. 11. The tumor destruction effects: (a) the fluorescence intensity of AlamarBlue was reduced by the Saos-2 tumor cells that were cultured on the various samples for 4 d after being treated with or without NIR irradiation and (b) the corresponding live/dead staining; (c) infrared thermographic photographs and (d) temperature elevation curve of ferric oxyhydroxide (FeOOH) and TR2-FeOOH in the osteosarcoma tissue (1.2 W/cm^2); (e) photographs of the tumor tissue, (f) time-dependent tumor-growth curves, (g) and time-dependent body weight curves after different treatments in nude mice; (h) and H&E, TUNEL, and Ki67 staining of the tumor tissue after different treatments.

group. All these pathological analyses suggested the best anti-tumor ability of TR2-FeOOH implant under NIR irradiation.

4. Conclusion

In this work, the Fe–OH bond breakage-mediated defects were fabricated on PEO/Mg–Fe LDH/FeOOH composite coating-modified Mg alloy via a thermal reduction process. The defects made in the coating led to a superhydrophobic state with antifouling and self-cleaning properties. Additionally, the superhydrophobic property of the coatings could be removed through immersion in a 75% ethanol solution. The coating substantially enhanced the corrosion resistance and biocompatibility of the raw Mg alloys. More importantly, the defect-rich coating exhibited superior PTT and CDT properties. The DFT calculation revealed that these properties were related to the narrower band gap of the defect-rich FeOOH, which lay above the Fermi level, with the smaller band in the near-infrared to visible light range and better H_2O_2 adsorption ability when compared to that of FeOOH. Because of the superior PTT and CDT abilities, the coating showed favorable NIR-induced antibacterial and antitumor performance. Overall, with switchable wettability, excellent corrosion resistance, and antibacterial and antitumor performance, this newly designed multi-functional coating is promising for OS therapy.

Notes

The authors declare no conflict of interest.

Declaration of interest statement

The authors declare no conflict of interest.

CRediT authorship contribution statement

Dongdong Zhang: Conceptualization, Methodology, Experiments (sample preparation and characterization, in vitro experiment, and in vivo experiment), Data curation, Writing – original draft, Writing – review & editing. **Ru Xu:** Conceptualization, Methodology, Writing – review & editing. **Shuhan Chen:** Writing – review & editing. **Huihui Du:** In vivo experiment. **Shi Qian:** Writing – review & editing. **Feng Peng:** Writing – review & editing, Supervision. **Xuanyong Liu:** Conceptualization, Methodology, Supervision, Writing – review & editing.

Appendix A. Supplementary data

Supplementary data to this article can be found online at https://doi.org/10.1016/j.bioactmat.2023.07.012.

References

[1] M. Kansara, M. Teng, M. Smyth, D. Thomas, Translation biology of osteosarcoma, Nat. Rev. Cancer 14 (2016) 722–735.

[2] M. Nathenson, P. Conley, E. Sausville, Immunotherapy: a New (and Old) approach to treatment of soft tissue and bone sarcomas, Oncol. 23 (2018) 71–83.

[3] S. Meltzer, J. Helman, New horizons in the treatment of osteosarcoma, N. Engl. J. Med. 385 (2021) 2066–2076.

[4] R. Grimer, Surgical options for children with osteosarcoma, Lancet Oncol. 6 (2005) 85–92.

[5] S. Magill, J. Edwards, W. Bamberg, Z. Beldavs, G. Dumyati, M. Kainer, R. Lynfield, L. Maloney, L. McAlliste, J. Nadle, S. Ray, D. Thompson, L. Wilson, S. Fridkin, Multistate point-prevalence survey of health care-associated infections, N. Engl. J. Med. 370 (2014) 1198–1208.

[6] C. Arciola, D. Campoccia, L. Montanaro, Implant infections: adhesion, biofilm formation and immune evasion, Nat. Rev. Microbiol. 16 (2017) 397–409.

[7] Y. Liu, Y. Zheng, X. Chen, J. Yang, H. Pan, D. Chen, L. Wang, J. Zhang, D. Zhu, S. Wu, K. Yeung, R. Zeng, Y. Han, S. Guan, Fundamental theory of biodegradable metals-definition, criteria, and design, Adv. Funt. Mater. 29 (2019), 1805402.

[8] X. Li, X. Liu, S. Wu, K. Yeung, Y. Zheng, P. Chu, Design of magnesium alloys with controllable degradation for biomedical implants: from bulk to surface, Acta Biomater. 45 (2016) 2–30.

[9] J. Wang, J. Xu, C. Hopkins, D. Chow, L. Qin, Biodegradable magnesium-based implants in orthopedics-A general review and perspectives, Adv. Sci. 7 (2020), 1902443.

[10] F. Peng, D. Zhang, X. Liu, Y. Zhang, Recent progress in superhydrophobic coating on Mg alloys: a general review, J. Magnesium Alloys 9 (2021) 1471–1486.

[11] C. Ding, Y. Liu, M. Wang, T. Wang, J. Fu, Self-healing, superhydrophobic coating based on mechanized silica nanoparticles for reliable protection of magnesium alloys, J. Mater. Chem. 4 (2016) 8041–8052.

[12] W. Yao, L. Wu, G. Huang, B. Jiang, A. Atrens, F. Pan, Superhydrophobic coatings for corrosion protection of magnesium alloys, J. Mater. Sci. Technol. 52 (2023) 100–118.

[13] L. Lv, Y. Xie, K. Li, T. Hu, X. Lu, Y. Gao, X. Zheng, Unveiling the mechanism of surface hydrophilicity-modulated macrophage polarization, Adv. Health. Mater. 7 (2021), 1800675.

[14] M. Li, M. Yao, W. Wang, P. Wan, X. Chu, Y. Zheng, K. Yang, Y. Zhang, Nitrogen-containing bisphosphonate-loaded micro-arc oxidation coating for biodegradable magnesium alloy pellets inhibits osteosarcoma through targeting of the mevalonate pathway, Acta Biomater. 121 (2021) 682–694.

[15] M. Chen, M. Wang, B. Li, D. Winston, W. Cheng, Y. Han, B. Lei, Visual and antibacterial magnesium implants with low biocorrosion and bioactive surface for in vivo tracking and treating MRSA infection, Chem. Eng. J. 417 (2021), 129198.

[16] N. Singh, U. Batra, K. Kumar, Progress in bioactive surface coatings on biodegradable Mg alloys: a critical review towards clinical translation, Bioact. Mater. 19 (2023) 717–757.

[17] M. Lopez-Lazaro, Dual role of hydrogen peroxide in cancer: possible relevance to cancer chemoprevention and therapy, Cancer Lett. 252 (2007) 1–8.

[18] X. Ren, D. Chen, Y. Wang, H. Li, Y. Zhang, H. Chen, X. Li, M. Huo, Nanozymes-recent development and biomedical applications, J. Nanobiotechnol. 20 (2022) 92.

[19] D. Zhang, S. Cheng, J. Tan, J. Xie, Y. Zhang, S. Chen, H. Du, S. Qian, Y. Qiao, F. Peng, X. Liu, Black Mn-containing layered double hydroxide coated magnesium alloy for osteosarcoma therapy, bacteria killing, and bone regeneration, Bioact. Mater. 17 (2022) 394–405.

[20] Y. Liu, T. Li, H. Ma, D. Zhai, C. Deng, J. Wang, S. Zhuo, J. Chang, C. Wu, 3D-printed scaffolds with bioactive elements-induced photothermal effect for bone tumor therapy, Acta Biomater. 73 (2018) 531–546.

[21] L. Sheng, Z. Zhang, Y. Zhang, E. Wang, B. Ma, Q. Xu, L. Ma, M. Zhang, G. Pei J. Chang, A novel "hot spring"-mimetic hydrogel with excellent angiogenic properties for chronic wound healing, Biomaterials 264 (2021), 120414.

[22] M. Chu, Y. Shao, J. Peng, X. Dai, H. Li, Q. Wu, D. Shi, Near-infrared laser light mediated cancer therapy by photothermal effect of Fe_3O_4 magnetic nanoparticles, Biomaterials 34 (2013) 4078–4088.

[23] D. Zhang, F. Peng, J. Tan, Y. Zhang, F. Wang, J. Xie, R. Xu, H. Du, S. Qian, Y. Qiao, M. Li, X. Liu, Self-assembled ferric oxyhydroxide nanosheet on PEO-coated magnesium alloy with photocatalytic/photothermal antibacterial and enhanced osteogenesis activities, Chem. Eng. J. 437 (2022), 135257.

[24] Z. Yin, W. Qi, R. Zeng, X. Chen, C. Gu, S. Guan, Y. Zheng, Advances in coating on biodegradable magnesium alloys, J. Magnesium Alloys 8 (2020) 42–65.

[25] D. Zhang, J. Zhou, F. Peng, J. Tan, X. Zhang, S. Qian, Y. Qiao, Y. Zhang, X. Liu, Mg-Fe LDH sealed PEO coating on magnesium for biodegradation control, antibacterial and osteogenesis, J. Mater. Sci. Technol. 105 (2022) 57–67.

[26] W. Zhang, D. Wang, Z. Sun, J. Song, X. Deng, Robust superhydrophobicity: mechanisms and strategies, Chem. Soc. Rev. 50 (2021) 4031–4061.

[27] K. Wang, H. Du, S. He, L. Liu, K. Yang, J. Sun, Y. Liu, Z. Du, L. Xie, W. Ai, W. Huang, Kinetically controlled, scalable synthesis of γ-FeOOH nanosheet arrays on nickel foam toward efficient oxygen evolution: the key role of in-situ-generated γ-NiOOH, Adv. Mater. 33 (2021), 2005587.

[28] Q. Wu, R. Yu, Z. Zhou, H. Liu, R. Jiang, Double core-shell structure $H-TiO_2/C/Fe_3O_4@rGO$ for Li^+ battery anodes with long cyclability, Appl. Surf. Sci. 559 (2021), 149975.

[29] L. Cui, R. Zeng, S. Guan, W. Qi, F. Zhang, S. Li, E. Han, Degradation mechanism of micro-arc oxidation coatings on biodegradable Mg-Ca alloys: the influence of porosity, J. Alloys Compd. (2017) 2464–2476.

[30] X. Hou, X. Huang, Z. Ai, J. Zhao, L. Zhang, Ascorbic acid/Fe@Fe_2O_3: a highly efficient combined Fenton reagent to remove organic contaminants, J. Hazard Mater. 310 (2016) 170–178.

[31] C. Du, Y. Zhang, Z. Zhang, L. Zhou, G. Yu, X. Wen, T. Chi, G. Wang, Y. Su, F. Deng, Y. Lv, H. Zhu, Fe-based metal organic frameworks (Fe-MOFs) for organic pollutants removal via photo-Fenton: a review, Chem. Eng. J. 431 (2022), 133932.

[32] X. Peng, J. Liu, C. Ming, B. Li, Z. Zhao, K. Ye, M. Zeng, R. Zou, X. Lu, J. Hu, $AgFeS_2$ nanoparticles as a novel photothermal platform for effective artery stenosis therapy, Nanoscale 12 (2020) 11288–11296.

[33] L. Jiao, W. Ye, Y. Kang, Y. Zhang, W. Xu, Y. Wu, W. Gu, W. Song, Y. Xiong, C. Zhu, Atomically dispersed N-coordinated Fe-Fe dual-sites with enhanced enzyme-like activities, Nano Res. 15 (2022) 959–964.

[34] Y. Chen, P. Wang, H. Hao, J. Hong, H. Li, S. Ji, A. Li, R. Gao, J. Dong, X. Han, M. Liang, D. Wang, Y. Li, Thermal atomization of platinum nanoparticles into